

Article

Preparation of Bimetallic CoFe@CSC-700 Carbonated Microspheres and Activated Peroxymonosulfate for Degradation of Levofloxacin

Tongke Hu ¹, Yazhen Chen ¹, Xiaolan Guo ¹, Yongjun Peng ¹ and Jianhua Cheng ^{1,2,*}

¹ Ministry of Education Key Laboratory of Pollution Control and Ecological Remediation for Industrial Agglomeration Area, School of Environment and Energy, South China University of Technology, Guangzhou 510006, China; hutongke611@163.com (T.H.); yzchen0114@163.com (Y.C.); lesleylh1@163.com (X.G.); jerry199916@163.com (Y.P.)

² South China Institute of Collaborative Innovation, Dongguan 523808, China

* Correspondence: jhcheng@scut.edu.cn

Abstract: The exploration of efficient, low-leaching, and recyclable transition-metal-based catalysts is of great importance for the removal of pollutants from peroxymonosulfate (PMS) in water purification processes. In this study, a bimetallic CoFe@CSC-700 composite was prepared by an alkaline gel pyrolysis reduction method using chitosan as a forming agent and applied to activate PMS to degrade levofloxacin (LEV). The leaching concentration of both cobalt and iron ions in the CoFe@CSC-700 catalyst was reduced by about 8-fold compared to the monometallic composite pellet catalyst. In addition, the removal efficiency of the CoFe@CSC-700 catalyst can still reach 90% after five cycles, showing good recyclability, recoverability and stability. Both free radical pathways ($\text{SO}_4^{\cdot-}$, $\cdot\text{OH}$, and $\cdot\text{O}_2^-$) and non-free radical pathways ($^1\text{O}_2$) were detected in the oxidation reaction, with free radical pathways as the main contributor. The possible degradation pathways of LEV were proposed by LC-MS tests. Overall, this study provides new insights into the construction of efficient and stable PMS catalysts for wastewater treatment.

Keywords: cobalt–iron bimetallic; chitosan carbonized microspheres; peroxymonosulfate; levofloxacin



Citation: Hu, T.; Chen, Y.; Guo, X.; Peng, Y.; Cheng, J. Preparation of Bimetallic CoFe@CSC-700 Carbonated Microspheres and Activated Peroxymonosulfate for Degradation of Levofloxacin. *Water* **2024**, *16*, 1818. <https://doi.org/10.3390/w16131818>

Academic Editor: Cidália Botelho

Received: 20 May 2024

Revised: 16 June 2024

Accepted: 21 June 2024

Published: 26 June 2024



Copyright: © 2024 by the authors. Licensee MDPI, Basel, Switzerland. This article is an open access article distributed under the terms and conditions of the Creative Commons Attribution (CC BY) license (<https://creativecommons.org/licenses/by/4.0/>).

1. Introduction

Water resource pollution has become a serious challenge globally with rapid economic development and the improvement of people's quality of life. In particular, the abuse and improper discharge of drugs have attracted extensive attention from numerous researchers and the public [1]. Levofloxacin (LEV), a third-generation fluoroquinolone, is a representative pollutant that is used on a large scale in aquaculture and agriculture, and the residues of this drug enter the environment through the food chain and have been detected in various river waters [2]. Its ecotoxicity in the aquatic environment is significant, and when organisms are exposed to LEV-containing water bodies, their behavioral patterns, growth rates, and reproduction may be adversely affected, thus posing significant potential risks to ecosystem stability and human health over time. Further, the presence of LEV in aqueous environments can also induce rapid genetic mutation in bacteria, leading to the development of drug-resistant bacteria [3]. However, LEV shows extreme resistance to traditional biological treatments and cannot be completely metabolized. Therefore, there is an urgent need to explore effective remediation technologies for removing LEV from aqueous environments.

Advanced oxidation processes (AOPs) based on sulfate radicals are an emerging technology that can effectively treat antibiotics in wastewater [4]. In recent years, the sulfate radical ($\text{SO}_4^{\cdot-}$) has garnered recognition as a technology with significant potential due to its high redox potential (2.5–3.1 V), long half-life, and wide pH use range [5,6]. Typically, $\text{SO}_4^{\cdot-}$

is generated from peroxymonosulfate (PMS) and peroxydisulfate (PDS). Considering the asymmetric molecular structure of PMS, it is easier to activate and produce sulfate radical ($\text{SO}_4^{\cdot-}$) than PDS [7]. There are many activation methods for PMS, including thermal activation [8], alkali activation [9], electrical activation [10], ultraviolet activation [11], transition metal activation [12] and ultrasonic activation [13]. The transition metal activation method is more applicable than other activation methods.

So far, Co-based metal oxides and their composites have attracted much attention among the many transition metals owing to their excellent catalytic properties [14]. However, the relatively high toxicity and potential carcinogenicity of Co leaching limit the practical application of Co in environmental remediation. Fe-based catalysts are considered as excellent alternatives for activating PMS because they are relatively environmentally friendly, widely available, and low-cost, but their catalytic performance is relatively low [15]. Previous studies have shown that when Co and Fe are combined, there is a synergistic catalytic effect, and Co-Fe bonding can reduce or even prevent Co^{2+} leakage. The study of Yang et al. [16] showed that the strong interaction between Co and Fe inhibited the leaching of Co^{2+} . The construction of bimetallic structures also improves the catalytic activity due to the synergistic effect between different metal species [17]. For example, Zhou et al. [18] found that the degradation efficiency of 2,4-dichlorophenol (2,4-DCP) in the $\text{FeCo}_2\text{O}_4/\text{PMS}$ system was higher than that in the monometallic oxide $\text{Fe}_3\text{O}_4/\text{PMS}$ system and $\text{Co}_3\text{O}_4/\text{PMS}$ system. Although many efficient catalysts available for the removal of organics have been reported, the unfavorable usability of powdered catalysts and metal leaching are still issues to be solved. Chitosan (CS) is a green biopolymer that has gradually attracted great interest due to its good molding properties and high biocompatibility [19]. Since CS chains are rich in $-\text{NH}_2$ and $-\text{OH}$ groups with high affinity for transition metals, many transition metals can be anchored to CS chains [20,21] and form magnetic chitosan microspheres in alkaline solutions, thus reducing metal loss and facilitating separation.

In this study, bimetallic CoFe@CSC-700 composites were designed and prepared by an alkaline gel pyrolytic reduction method to address the unfavorable recoverability of powder catalysts and metal leaching. Using LEV as the target pollutant, the catalytic activity of the $\text{CoFe@CSC-700}/\text{PMS}$ system was systematically investigated, and the influencing factors (solution pH, catalyst dosing, PMS concentration) and the effects of different water quality components were explored. In addition, the recycling stability and recoverability of CoFe@CSC-700 were evaluated, and the reactive oxygen species (ROS) in the reaction system and reaction mechanism were described. Finally, the intermediates of LEV degradation were also elucidated by LC-MS, and the degradation pathways of the reaction were considered. Theoretical support and a practical application basis were provided to promote the activation of PMS by bimetallic composites for the purification of water pollutants.

2. Materials and Methods

2.1. Materials

Levofloxacin (LEV, $\geq 98.0\%$) was purchased from Sigma-Aldrich Co., Ltd. (Shanghai, China). Cobalt chloride hexahydrate ($\text{CoCl}_2 \cdot 6\text{H}_2\text{O}$, $\geq 99.0\%$), ferric chloride hexahydrate ($\text{FeCl}_3 \cdot 6\text{H}_2\text{O}$, $\geq 99.0\%$), peroxymonosulfate ($\text{KHSO}_5 \cdot 0.5\text{KHSO}_4 \cdot 0.5\text{K}_2\text{SO}_4$, PMS), methanol (MeOH, HPLC, $\geq 99.9\%$), tert butyl alcohol (TBA), L-histidine (L-His), and p-Benzoquinone (p-BQ) were purchased from Shanghai Macklin Biochemical Technology Co., Ltd. (Shanghai, China). Chitosan (CS, 95.0% deacetylation), sulfuric acid (H_2SO_4 , 95~98%), acetic acid (CH_3COOH , 99%), sodium acetate (CH_3COONa , $\geq 99\%$), sodium hydroxide (NaOH, $\geq 98\%$), sodium chloride (NaCl), sodium nitrate (NaNO_3), and sodium sulfate (Na_2SO_4) were supplied by Aladdin Biochemical Technology Co., Ltd. (Shanghai, China). Humic acid ($\geq 90\%$) used as natural organic matter (NOM) was provided by Sinopharm Chemical Reagent Beijing Co., Ltd. (Beijing, China). All reagents were not purified and were used directly. Ultrapure water ($18.2 \text{ M}\Omega \cdot \text{cm}$) from the Milli-Q system was used to prepare solutions in all experiments. The river water in this study was taken from the Pearl River.

2.2. Characterization

The phases of the products were characterized by X-ray powder diffraction (XRD, Bruck D8 Advance, Hersbruck, Germany). Scanning electron microscopy (SEM) images were acquired (FE-SEM, ZEISS ULTRA 55, Oberkochen, Germany). The microstructure and crystal structure of the prepared materials were studied by high-resolution transmission electron microscopy (HRTEM, FEI Tecnai TF-20, Hillsboro, OR, USA) under 200 kV voltage. Raman spectra were measured with a Raman microscope (Raman, Renishaw Invia RAMA, Wotton-under-Edge, UK), and the excitation wavelength was 532 nm. The elemental and surface valence states of the synthesized materials were measured by X-ray photoelectron spectroscopy (XPS, Thermo Scientific Nexsa, Waltham, MA, USA). An Inductively Coupled Plasma Mass Spectrometer was used to measure the concentration of iron and cobalt ions (ICP-MS, Agilent 7700, Santa Clara, CA, USA). An electron paramagnetic resonance spectrometer (EPR, Bruker A300, Rheinstetten, Germany) was used to identify the type of reactive oxygen species. The intermediates during the LEV degradation process were identified by liquid chromatography–mass spectrometry (LC/MS, Agilent 1290 Infinity/6460, Santa Clara, CA, USA).

2.3. Preparation of CoFe@CSC-X Carbonized Microspheres

Firstly, 2 mL of acetic acid and 2 g of CS were added to 100 mL of deionized water and stirred to dissolve them completely. Then, an aqueous metal solution with a Fe concentration of 0.5 mol/L and a Co/Fe ratio of 1:1 was prepared from $\text{CoCl}_2 \cdot 6\text{H}_2\text{O}$ and $\text{FeCl}_3 \cdot 6\text{H}_2\text{O}$, and then this solution was added to the above CS solution at a volume ratio of 1:10 and stirred for 30 min; the mixture was recorded as solution A. NaOH and CH_3COONa were dissolved in deionized water with stirring at a ratio of 1.25 M/0.1 M to obtain another solution, which was recorded as solution B. Solution A was injected into 80 °C solution B via syringe, forming reddish-brown gel microspheres. After 2 h of hardening, the microspheres were washed to neutrality with deionized water and oven-dried at 80 °C for 12 h. The resulting microsphere material was recorded as CoFe@CS. CoFe@CS microspheres were then calcined at different calcination temperatures (600 °C, 700 °C, and 800 °C) under a nitrogen atmosphere for 2 h to prepare CoFe@CSC-X, where X denotes the temperature. Similar to the preparation of CoFe@CS microspheres, CS microspheres were successfully prepared without incorporating the metal solution. At the same time, Co@CS microspheres were prepared by replacing $\text{FeCl}_3 \cdot 6\text{H}_2\text{O}$ with $\text{CoSO}_4 \cdot 7\text{H}_2\text{O}$, and Fe@CS microspheres were prepared by replacing $\text{CoCl}_2 \cdot 6\text{H}_2\text{O}$ with $\text{FeSO}_4 \cdot 7\text{H}_2\text{O}$. Under the same conditions as those used for the preparation of CoFe@CSC-X, the products of the calcination of the above three microspheres were named CSC microspheres, Co@CSC microspheres, and Fe@CSC microspheres, respectively.

2.4. Evaluation of the Catalytic Performance

In all batch experiments, 250 mL conical flasks containing 100 mL of LEV solution (10 mg/L) at pH = 6.8 (initial pH) were placed on a shaker (180 rpm, 298 K) to evaluate the catalytic performance. The initial pH of the reaction solution was unadjusted unless otherwise specified. When discussing the effect of initial pH on degradation, the initial pH of the solution could be adjusted to the desired pH with 1 M H_2SO_4 or NaOH solution. A certain amount of catalyst and PMS were simultaneously introduced into the conical flask to initiate the catalytic reaction. At regular time intervals, 1 mL of sample was taken at each time during the reaction, and the solution was filtered through a 0.22 μm filter membrane. Next, 0.5 mL of methanol was immediately injected into sampling bottles to quench the free radical reaction and redundant oxidant. The used catalysts were collected with a magnet and washed alternately with deionized water and ethanol to remove residual organics for repeatability and stability tests. All the experiments were repeated three times, and the average value was taken as the data results.

2.5. Analytical Method

In all experiments, the concentration of LEV was quantified by high-performance liquid chromatography (HPLC) using the standard working curve method. The mobile phase consisted of 20% chromatographic grade acetonitrile and 80% ultrapure water containing 0.3% formic acid in a 10 μ L injection volume at a flow rate of 1 mL/min with a detection wavelength of 290 nm.

3. Results

3.1. Catalyst Characterization

The SEM results showed the surface morphology of the catalysts. As shown in Figure 1a, the CoFe@CSC-700 crystals were shaped as microspheres with a diameter of about 1 μ m, and the surface of the uncalcined CoFe@CS (Figure 1d) was folded, which was presumed to be the wrapped chitosan molecular chain. After CoFe@CS was calcined at 700 $^{\circ}$ C, the wrapped chitosan volatilized at high temperature, more voids appeared on the surface of the spheres, and some of the internal cobalt–iron complexes were revealed, as shown in Figure 1b,c. Meanwhile, the microstructure of CoFe@CSC-700 was characterized by TEM. As shown in Figure 1e,f, the sample has an obvious “core–shell” structure. In Figure 1f–i, the typical lattice stripes of graphitic carbon shells are obvious, indicating the presence of graphitized carbon shells. According to Figure 1g,h, the lattice spacing of the ‘core’ can be calculated, and the results match the (110), (200) and (211) planes of the CoFe alloy. In summary, it can be seen that the CoFe alloy particles were encapsulated within the graphitic carbon shell that was embedded in the graphitic carbon matrix, which reduced the clustering of CoFe alloy particles and enhanced electron mobility [22,23]. Meanwhile, the graphitic carbon matrix can serve as a protective layer for the CoFe alloy particles, protecting them from oxidation and corrosion, which improves the stability of the composites [24]. In addition, the combined EDX spectra showed the elemental distributions, as shown in Figure 1i, for C, N, O, Fe, and Co. Obviously, the range of C and N elements did not differ much, indicating the partial doping of the carbon matrix with N. Meanwhile, the same distribution of Co and Fe elements indicated the successful synthesis of CoFe alloy.

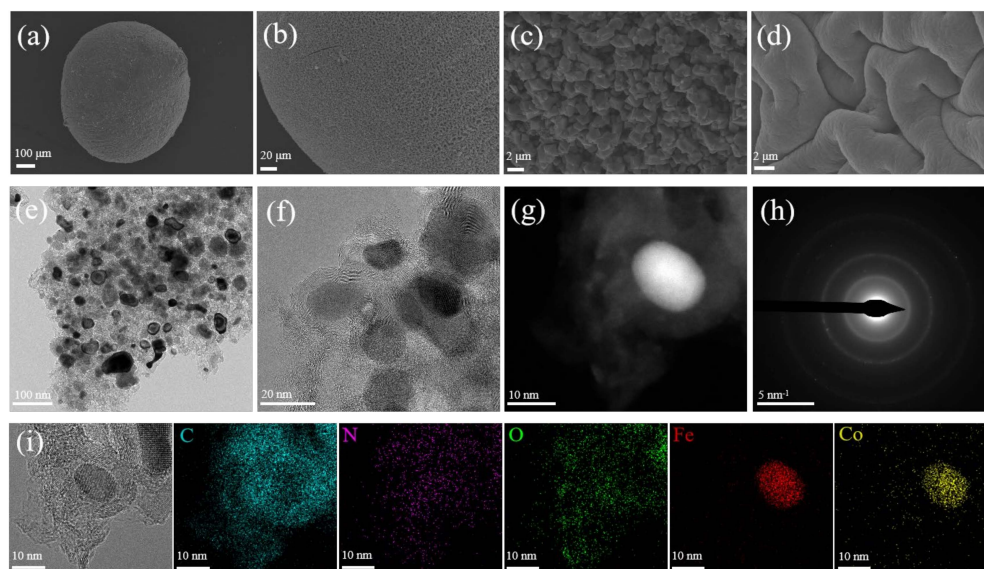


Figure 1. (a–c) SEM images of CoFe@CSC-700; (d) SEM image of CoFe@CS; (e,f) CoFe@CSC-700 TEM images; (g) HRTEM images; (h) SAED images; (i) EDX images and corresponding surface scan images of elements of C, N, O, Fe, and Co.

XRD analyses were performed to clarify the crystal structure and composition of the catalysts. As shown in Figure 2a, characteristic peaks of CoFe@CSC-600, CoFe@CSC-700, and CoFe@CSC-800 at 44.8 $^{\circ}$, 65.3 $^{\circ}$, and 82.7 $^{\circ}$ were typical of the (110), (200), and (211)

lattice planes assigned to CoFe alloys (PDF# 49-1567). It is possible that CoFe@CS was calcined under a N_2 atmosphere under higher temperature conditions when the metal center was reduced to a lower oxidation state, resulting in CoFe alloys [25]. The CoFe@CSC-700 characteristic peaks had the highest intensities, whereas the diffraction peak intensities of CoFe alloys were changed by changing the calcination temperature, suggesting that the degree of crystallinity was affected by the temperature to a certain extent. In addition, an extra characteristic peak can be observed in the XRD pattern of CoFe@CSC-700, which is known from the literature to be a broad peak at 26.3° attributable to the (002) diffraction plane of graphitized carbon [24,26], which corresponds to the previous TEM results.

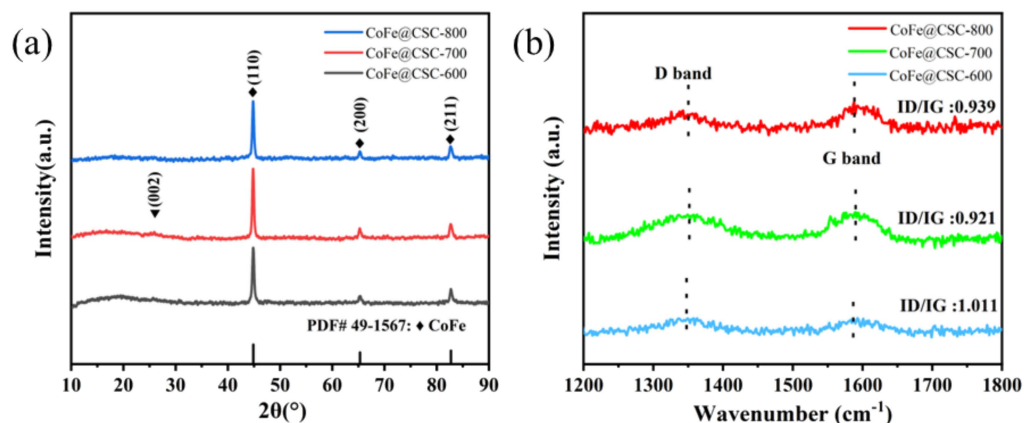


Figure 2. (a) XRD patterns of CoFe@CSC-600, CoFe@CSC-700, and CoFe@CSC-800; (b) Raman spectra of CoFe@CSC-600, CoFe@CSC-700, and CoFe@CSC-800.

To explore the degree of graphitization at various calcination temperatures, Raman spectroscopy was conducted. The Raman results exhibited two distinctive peaks positioned approximately at 1350 cm^{-1} and 1580 cm^{-1} , which were attributed to the D and G bands, respectively. The D band indicated the contribution of sp^3 defects in the carbon, i.e., the presence of defects or disorder [27], whereas the G band was attributed to the stretching of the C-C bonds within the graphite structure [28], which was related to the graphitized carbon of the material [24]. Therefore, the degree of graphitization of the material can be expressed by the I_D/I_G intensity ratio. The smaller this ratio was, the higher the degree of graphitization was. As shown in Figure 2b, the I_D/I_G ratio values for CoFe@CSC-600, CoFe@CSC-700, and CoFe@CSC-800 were 1.011, 0.921, and 0.939, respectively. With the increase in calcination temperature, the I_D/I_G ratio decreased and then increased, and it was lowest at 700°C , indicating that the degree of graphitization would be damaged if the temperature was too high [26]. This indicated that the Raman experimental results also corresponded to the experimental results of XRD.

In order to investigate the elemental composition and valence distribution of the CoFe@CSC-700 surface, the catalyst was analyzed by XPS. Firstly, the CoFe@CSC-700 consists of C, O, N, Fe, and Co elements, as seen in the survey spectrum (Figure 3a), which was compatible with the EDX results. Figure 3b shows the high-resolution C1s energy spectra obtained from the test, which corresponded to the C-C characteristic peak at 284.8 eV binding energy, the C-N bond characteristic peak at 285.7 eV binding energy, the C=O bond characteristic peak at 288.1 eV , and the O-C=O bond characteristic peak at 290.0 eV , as shown in the past literature [29], whereas the π - π vibration of carbon corresponds to the π - π vibration at 291.6 eV . The incorporation of C-N bonds indicated that nitrogen had been successfully doped into the carbon molecular structure, constituting a crucial facet of the redox reaction process [30]. The concurrent presence of nitrogen-doped graphitic carbon alongside CoFe alloys can enhance the electron mobility between the metallic components and PMS [31]. The high-resolution energy level spectrum of N 1s for CoFe@CSC-700 (Figure 3c), can be categorized into three separate peaks. The binding energies of these peaks were 398.6 eV , 400.7 eV , and 402.5 eV , which were attributed to

pyridine N, pyrrole N, and graphite N. As shown in Figure 3d, the O 1s XPS high-resolution energy spectrum can be fitted to three distinct peaks, the peaks of M-O (lattice oxygen), M-O-H (adsorbed oxygen), and impurity water, which are located at 530.4 eV, 532.3 eV, and 534.7 eV, respectively [32]. Figure 3e demonstrates the electronic state characteristics of Fe 2p, which specifically consists of two spin orbitals, Fe 2p_{1/2} and Fe 2p_{3/2}. The peak at 707.4 eV corresponds to the characteristic peak of Fe⁰, 711.0 eV and 724.2 eV correspond to the characteristic peaks of Fe^{II}, 713.8 eV and 726.3 eV are the characteristic peaks of Fe^{III}, and the peak at 719.7 eV corresponds to the satellite peaks of Fe. The high-resolution spectra of Co 2p (Figure 3f) consist mainly of the peaks at Co^{II} at 782.7 eV and 797.1 eV and Co^{III} at 780.3 eV and 795.4 eV, as well as two satellite peaks at 787.0 eV and 803.4 eV. There are five valence states of Fe⁰/≡Fe^{II}/≡Fe^{III} and ≡Co^{II}/≡Co^{III} on the surface of the two elements, and the presence of multiple valence states is favorable for electron transfer according to the redox potentials of Fe cobalt. According to the redox potential of cobalt-iron, the existence of multiple valence states is favorable for electron transfer, and a redox cycle of ≡Fe^{II}/≡Fe^{III} and ≡Co^{II}/≡Co^{III} can exist to accelerate the activation of PMS.

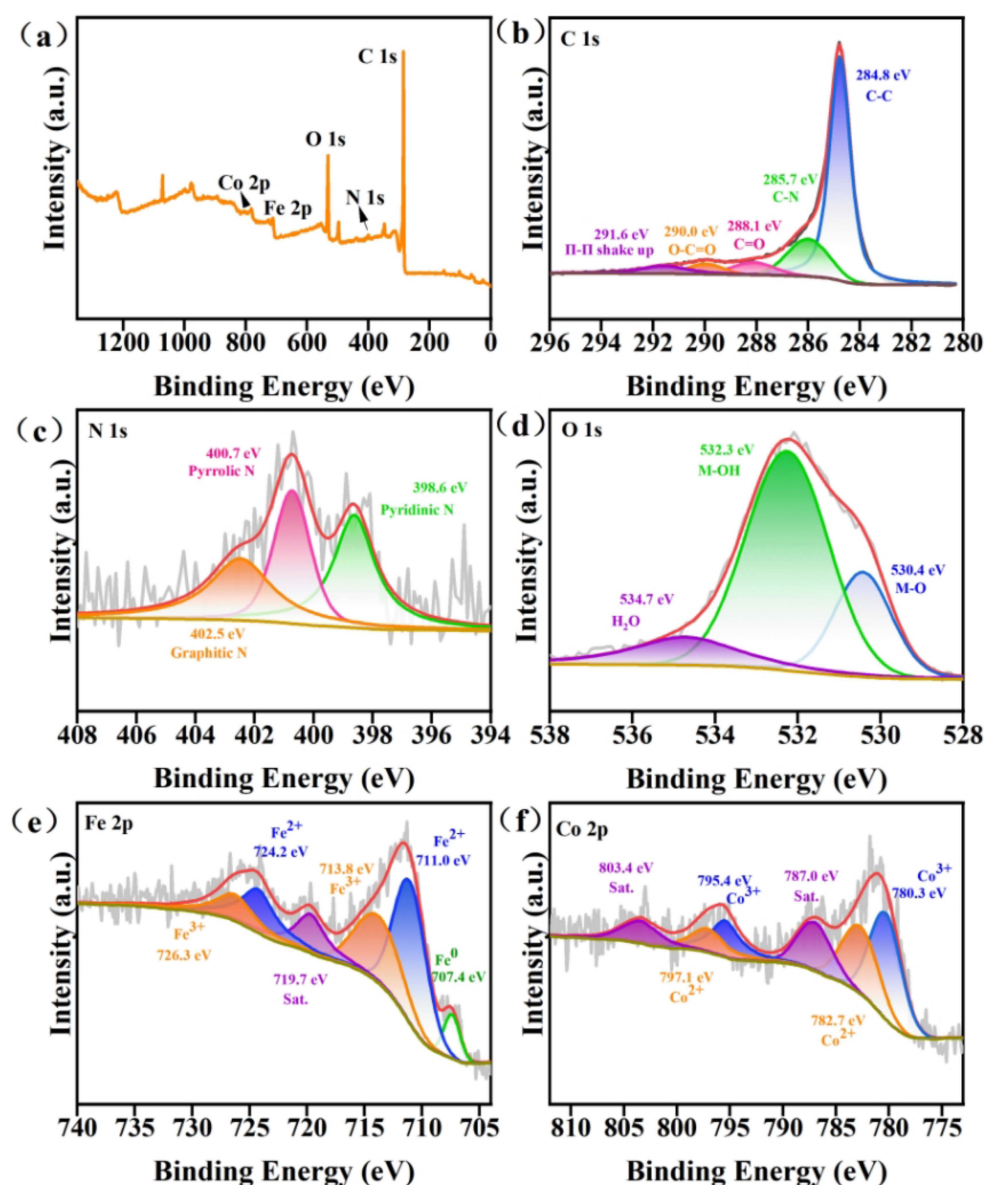


Figure 3. (a) Wide XPS spectrum of CoFe@CSC-700; (b) C 1s spectra; (c) N 1s spectra; (d) O 1s spectra; (e) Fe 2p spectra; (f) Co 2p spectra.

3.2. Catalytic Performance

In order to investigate the practical effects of the five different catalysts prepared (CSC-700, Co@CSC-700, Fe@CSC-700, CoFe@CSC-700, and CoFe@CS) applied for the degradation of LEVs by activated PMS and to select the best-performing samples for the subsequent experiments, firstly, adsorption experiments were carried out without the addition of PMS, and the results are shown in Figure 4. When CSC-700, Co@CSC-700, Fe@CSC-700, CoFe@CSC-700, and CoFe@CS were used alone, none of them adsorbed more than 10% of LEV within 30 min, so the adsorption capacity of these five materials was negligible during the whole degradation process. The effect of the five different catalysts prepared on the removal of LEV within the PMS system was mainly a degradation effect rather than an adsorption effect.

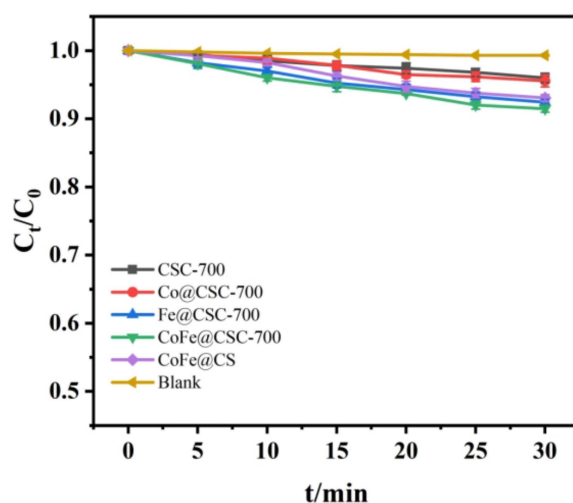


Figure 4. Adsorption effect of different catalysts on LEV.

Based on the results of the above adsorption experiments, the degradation performance of PMS activated by the above five different chitosan microspheres was compared without considering the effect of adsorption effect on LEV degradation. An investigation of the degradation performance without catalyst addition and with pure PMS addition was also carried out. As shown in Figure 5, when there was only pure PMS without a catalyst in the system, PMS alone degraded only 2% of LEV within 30 min, which indicated that PMS alone basically could not generate free radicals and its degradation effect was negligible. When both CSC-700 and PMS were present, there was no significant increase in LEV removal, indicating that CCM was ineffective against PMS. When Co@CSC-700, Fe@CSC-700, CoFe@CSC-700, and CoFe@CS were used as catalysts, the LEV removal rates were 99.8%, 29.3%, 99.9%, and 44.1%, respectively. It can be seen that the combination of Co@CSC-700 and CoFe@CSC-700 with PMS significantly improved the LEV degradation efficiency, reaching 99.9% removal within 30 min. These results unequivocally demonstrated that the carbonated Co@CSC-700 and CoFe@CSC-700 presented a greater number of active sites than the uncarbonated CoFe@CS, whereas Fe@CSC-700 was not as effective as the uncarbonated CoFe@CS, probably due to the presence of cobalt, which had stronger catalytic activity than iron [33]. Compared to the monometallic catalyst Fe@CSC-700, CoFe@CSC-700 clearly had superior catalytic performance; while Co@CSC-700 was certainly also catalytic, its reaction rate was smaller than that of CoFe@CSC-700, confirming the cooperative catalytic impact of Co and Fe. Meanwhile, considering the environmental goodness of the materials, inductively coupled plasma mass spectrometry (ICP-MS) was utilized for determining the concentration of cobalt ions and iron ions leached out from the solution at the end of the reaction for the three systems Co@CSC-700/PMS, Fe@CSC-700/PMS, and CoFe@CSC-700/PMS. The results showed that the leaching of cobalt ions from Co@CSC-700/PMS was up to 3.33 mg/L, and that of iron ions from Fe@CSC-700/PMS was up to 0.85 mg/L. The

leaching of cobalt ions and iron ions from CoFe@CSC-700 decreased to 0.43 mg/L and 0.10 mg/L, and these values were reduced by about 8 times; this result was lower than the requirements of the national standard (GB3838-2002) [34]. Additionally, this finding reaffirmed the cooperative catalytic impact of Co and Fe, and the Co/Fe coupling could inhibit ion leaching [16]. Considering the performance, environmental soundness, and reusability, CoFe@CSC-700 was used in this study to carry out the following experiments related to the influence of environmental factors and so on.

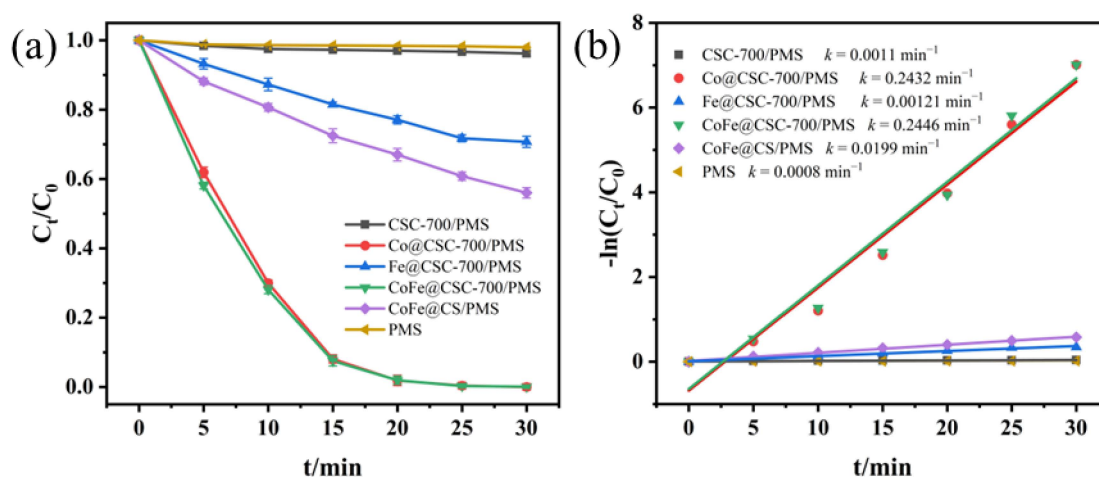


Figure 5. (a) Comparison of the effects of LEV degradation in different conditions; (b) reaction constants of LEV degradation.

It is well known that the state of presence of contaminants and the surface charge of the catalyst are affected by the solution pH, which in turn affects the PMS system reaction process. In our study, the point of zero charge (pH_{PZC}) was determined by measuring the zeta potential of the catalyst surface, which represents the pH of the solution when the net surface charge of the material is zero [35]. As shown in Figure S1, the pH_{PZC} of CoFe@CSC-700 was 6.28, the catalyst surface is positively charged when the pH of the solution < 6.28 and negatively charged at $\text{pH} > 6.28$. The dissociation constants of the LEV molecule in water are $\text{pK}_{\text{a}1} = 6.02$ and $\text{pK}_{\text{a}2} = 8.15$, respectively. It usually exists in water in the cationic form ($\text{pH} < 6.02$), the amphoteric form ($6.02 < \text{pH} < 8.15$), and the anionic form ($\text{pH} > 8.5$). Figure 6 shows the degradation of LEV by the CoFe@CSC-700/PMS system at different pH conditions. The degradation efficiency of LEV can reach more than 99% when the pH ranges from 3.0 to 6.8, and overall, the degradation rate was faster when it was acidic. Although the surface charge distributions of the catalyst and the pollutant were essentially similar in the acidic pH range and there was electrostatic hindrance, the release of cobalt–iron ions increased with decreasing pH, thus accelerating the catalytic reaction. Therefore, the decrease in LEV degradation rate in systems with pH ranging from 3.0 to 6.8 may be caused by a decrease in cobalt iron dissolution. When the pH was further increased (6.8–11.0), the degradation of LEV decreased continuously. In particular, the degradation effect on LEV decreased to 56% at pH 11.0. This was due to the fact that both catalyst and pollutant surfaces were negatively charged, and the electrostatic effect may have hindered the reaction process between CoFe@CSC-700 and LEV. In summary, considering the removal effect and convenience, the initial pH of 6.8 was chosen for the experiments in this study.

As shown in Figure 7, the effects of different catalyst dosages (30–130 mg/L) on the catalytic degradation of LEV in the CoFe@CSC-700/PMS system were investigated. The degradation efficiency of LEV increased from 42% to more than 99% when the catalyst dosage was increased from 30 mg/L to 130 mg/L. When the catalyst dosage was increased from 100 to 130 mg/L, the overall LEV removal rate was basically the same, but the degradation rate was slightly slower. On one hand, a higher catalyst dosage can provide

more active sites for activating the PMS reaction for LEV removal [36,37]. On the other hand, at a certain concentration of PMS, excessive catalyst dosage may compete for the reaction with PMS and inhibit the rate of formation of reactive oxygen components. The appropriate amount of catalyst was necessary to obtain the excellent performance of the reaction system, so the CoFe@CSC-700 dosage of 100 mg/L (0.1 g/L) was selected in the subsequent experiments considering the effect and economic cost.

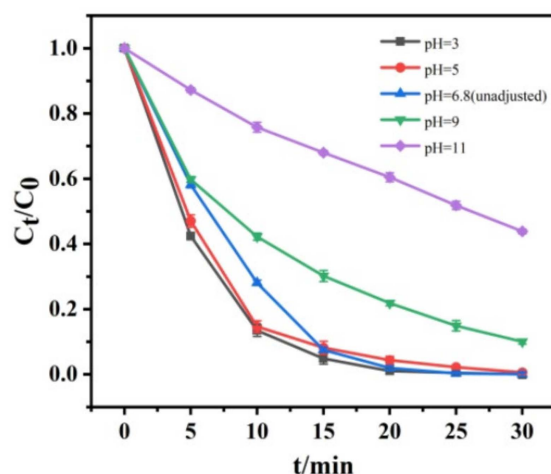


Figure 6. PMS system with CoFe@CSC-700 at different initial pH values to solve LEV rendering.

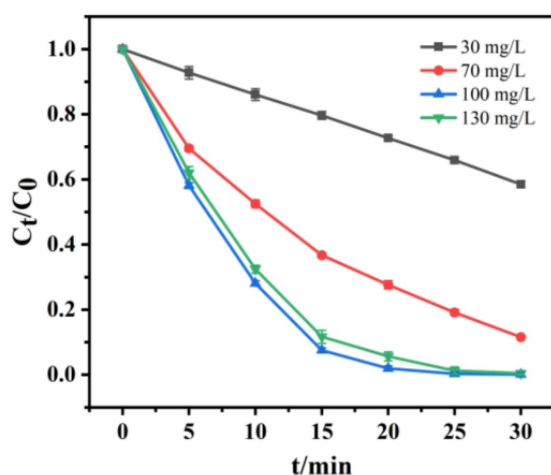


Figure 7. PMS system with CoFe@CSC-700 at different initial PMS concentrations to solve LEV rendering.

The concentration of PMS plays a significant role in the efficiency of LEV removal. Figure 8 shows the degradation curves of LEV in the reaction system when different concentrations of PMS were added. The LEV degradation efficiency of the CoFe@CSC-700/PMS system continued to increase with the increase in PMS concentration from 25 mg/L to 100 mg/L and reached a peak at a PMS concentration of 100 mg/L, which was attributed to the fact that a larger concentration of PMS could provide more free radicals for the reaction. However, when the PMS concentration was further escalated, the LEV removal rate remained nearly consistent. This result was due to the fact that at a fixed catalyst dosage, an increase in PMS concentration led to self-scavenging between free radicals [38,39]. Therefore, a concentration of PMS of 100 mg/L (0.1 g/L) was chosen for the reaction in the subsequent experiments.

In the complex environment of natural waters, a diverse range of anions and naturally organic compounds are present, which may have an impact on the chemical reaction process through competitive interactions with the target pollutants or by inducing the generation of novel free radicals. In this study, we selected three ubiquitous inorganic

anions (Cl^- , NO_3^- , SO_4^{2-}) and typical humic acid (HA) to investigate the effect of co-existing components in the system on the removal of LEV by the CoFe@CSC-700/PMS system. As shown in Figure 9, the high concentration of Cl^- had a large inhibitory effect on the catalytic degradation by PMS, and the 10 mM Cl^- concentration caused the degradation efficiency of LEV to decrease from 99.9% to 84.1% within 30 min. This change in degradation efficiency could be caused by two reasons. On one hand, Cl^- consumed highly active $\cdot\text{OH}$ and $\text{SO}_4\cdot^-$ in the CoFe@CSC-700/PMS system and generated low-activity $\text{Cl}\cdot$ (Equation (1)) and $\text{ClOH}\cdot^-$ (Equation (2)). On the other hand, the reaction of Cl^- and HSO_5^- generated HOCl (Equation (3)) and Cl_2 (Equation (4)), leading to a decrease in the production of $\cdot\text{OH}$ and $\text{SO}_4\cdot^-$ in the CoFe@CSC-700/PMS system [40]. In addition, it can also be seen from the figure that the addition of NO_3^- and SO_4^{2-} slightly inhibited LEV removal at a concentration of 10 mM, with LEV removal reduced by 5.1% and 6.2%, respectively. The reduced degradation efficiency indicated that they competed with the target pollutants (Equations (5)–(7)). However, they reacted slowly with $\cdot\text{OH}$ and $\text{SO}_4\cdot^-$, so they had little effect on the presence of $\cdot\text{OH}$ and $\text{SO}_4\cdot^-$ in the system [41,42]. In addition to the anions mentioned above, natural organic matter (NOM) is also present in natural water. HA is one of the common forms of NOM, and its effect on the CoFe@CSC-700/PMS system is also significant. The inhibitory effect of HA on LEV degradation decreased to 86.2% with the addition of HA (Figure 9), which was attributed to the fact that HA, with its rich electronic structure, competes with LEV for $\cdot\text{OH}$ and $\text{SO}_4\cdot^-$, thus inhibiting LEV degradation [43,44]. In summary, the order of inhibition of LEV degradation by different water quality backgrounds was $\text{Cl}^- > \text{HA} > \text{SO}_4^{2-} > \text{NO}_3^-$.

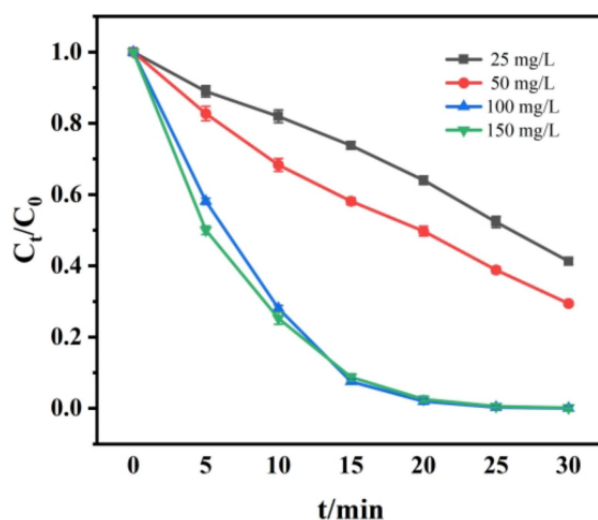
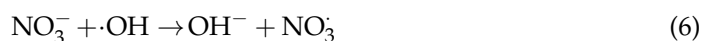
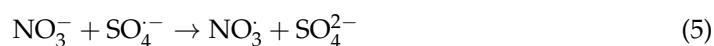
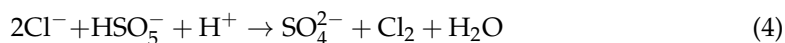


Figure 8. PMS system with CoFe@CSC-700 at different concentrations of PMS to solve LEV rendering.

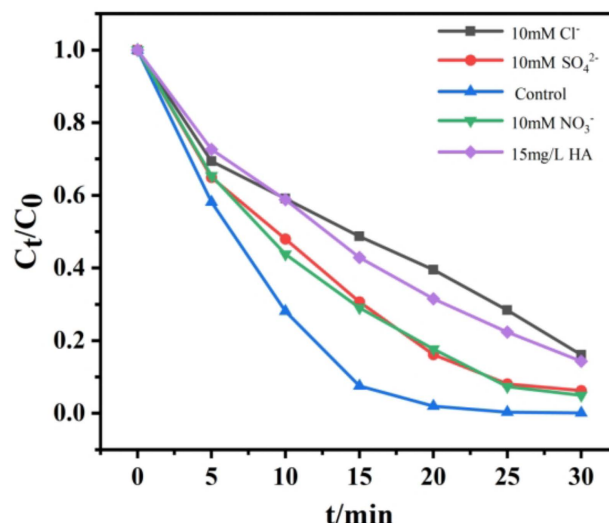


Figure 9. Effect of Cl^- , NO_3^- , SO_4^{2-} , and HA on LEV degradation in the CoFe@CSC-700/PMS system.

3.3. Evaluation of the Stability and Performance of CoFe@CSC-700

The reusability and stability of the catalyst are the key investigation index; in order to explore this performance, CoFe@CSC-700 cyclic reaction experiments were carried out. After each cyclic reaction, the catalyst was washed with water and ethanol and vacuum-dried for reuse. From Figure 10a, it can be seen that the degradation rate of CoFe@CSC-700 for LEV can still be maintained above 90% after five degradation cycles, which indicates that CoFe@CSC-700 was stable in nature. From Section 3.2, it can be seen that the leaching value of cobalt and iron ions in CoFe@CSC-700 was lower than the national standard, but the leaching of metal ions led to the loss of the active site, and thus there was a slight decrease in the catalytic efficiency after five cycles of the experiment. Also, the decrease in catalytic efficiency during cycling was related to the coverage of active sites on the surface of the CoFe@CSC-700 catalyst by degradation intermediates [45]. In addition to the consideration of catalyst efficiency, the more difficult recovery of catalyst materials in water is the key issue that leads to the inability to reuse in the current practical application of the PMS process, which will increase the cost of use. From Figure 10b, it can be seen that CoFe@CSC-700 had a saturation magnetization of 96.12 emu/g. Therefore, the catalyst and the water can be separated very quickly under the application of a magnetic field, which can save costs in practical applications. In addition, as shown in Figure 10c, the XRD results before and after the reaction indicated that the crystal structure and elemental composition of the CoFe@CSC-700 catalyst remained stable, and the slight change in the peak intensity of the XRD could be caused by the loss of metal ions. This further indicated that CoFe@CSC-700 has good reusability and high water stability in the PMS reaction system and has strong potential for environmental applications. Table S1 listed the performance comparison of CoFe@CSC-700 with other previously reported catalysts for LEV degradation [46–52]. As can be seen from Table S1, CoFe@CSC-700 was able to achieve a higher LEV removal rate in a shorter period at a lower catalyst dosage and PMS concentration than the catalysts prepared in other studies, suggesting that the catalyst has superior performance and greater potential application prospects for treating LEV pollution in water.

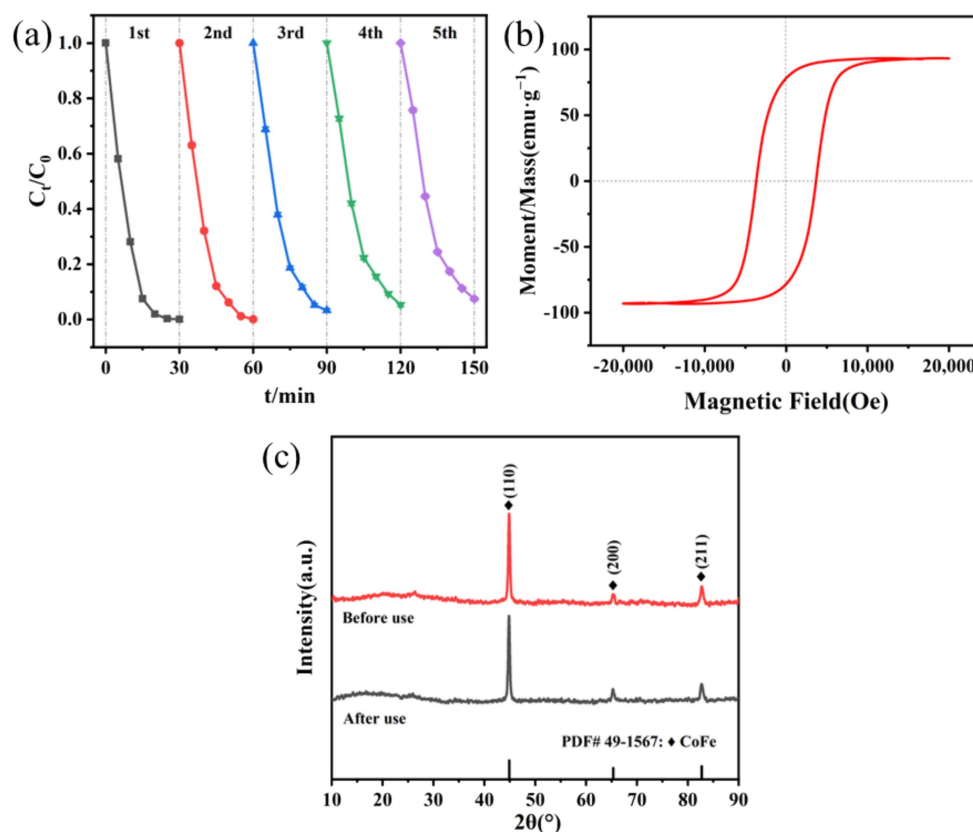


Figure 10. (a) The degradation effect of CoFe@CSC-700/PMS system on LEV in 5 cycles; (b) the hysteresis loop of CoFe@CSC-700; (c) XRD comparison before and after use of CoFe@CSC-700/PMS.

3.4. Identification of ROS and Proposed Catalytic Mechanism

The degradation mechanism of the LEV in the CoFe@CSC-700/PMS system was investigated by free radical quenching experiments, which were able to reveal the types of ROS that removed LEV and the extent of their contribution. In these experiments, sufficient amounts of the corresponding specific quenchers were added at the beginning of the reaction to determine the effect of the main ROS on LEV degradation, while the other experimental conditions were kept constant. MeOH was chosen as the quencher for $\text{SO}_4^{\cdot-}$ and $\cdot\text{OH}$ because of the high reaction rates ($K_{\text{SO}_4^{\cdot-}} = (1.6 \sim 7.7) \times 10^7 \text{ M}^{-1}\text{S}^{-1}$, $K_{\cdot\text{OH}} = (1.2 \sim 2.8) \times 10^9 \text{ M}^{-1}\text{S}^{-1}$). Also, TBA, p-BQ, and L-His were also employed as quenchers corresponding to $\cdot\text{OH}$, $\cdot\text{O}_2^-$, and $^1\text{O}_2$, respectively, with corresponding reaction rates of $(3.8 \sim 7.6) \times 10^8 \text{ M}^{-1}\text{S}^{-1}$, $(0.9 \sim 1.0) \times 10^9 \text{ M}^{-1}\text{S}^{-1}$, and $5 \times 10^7 \text{ M}^{-1}\text{S}^{-1}$, respectively [53,54]. As shown in Figure 11d, the removal of LEV reached 99.9% within 30 min of the reaction without the addition of a quencher, while the addition of TBA and MeOH resulted in LEV removals of 55.8% and 16.3%, respectively. The results showed that both $\text{SO}_4^{\cdot-}$ and $\cdot\text{OH}$ played significant roles in the LEV degradation reaction with comparable contribution importance. After the addition of p-BQ, the degradation rate of LEV decreased to 57.2%, indicating that $\cdot\text{O}_2^-$ is another important active species. Compared with the above quenchers, the degradation rate of LEV decreased to 82.8% after the addition of L-His, which had the least inhibitory effect on the catalytic activity in the CoFe@CSC-700/PMS system, but the contribution of $^1\text{O}_2$ to the degradation of LEV could not be neglected. In summary, the results showed that $\text{SO}_4^{\cdot-}$, $\cdot\text{OH}$, $\cdot\text{O}_2^-$, and $^1\text{O}_2$ were all involved in the degradation process of LEV in the CoFe@CSC-700/PMS system, in which $\text{SO}_4^{\cdot-}$, $\cdot\text{OH}$, and $\cdot\text{O}_2^-$ played the dominant roles, and $^1\text{O}_2$ also contributed to LEV degradation.

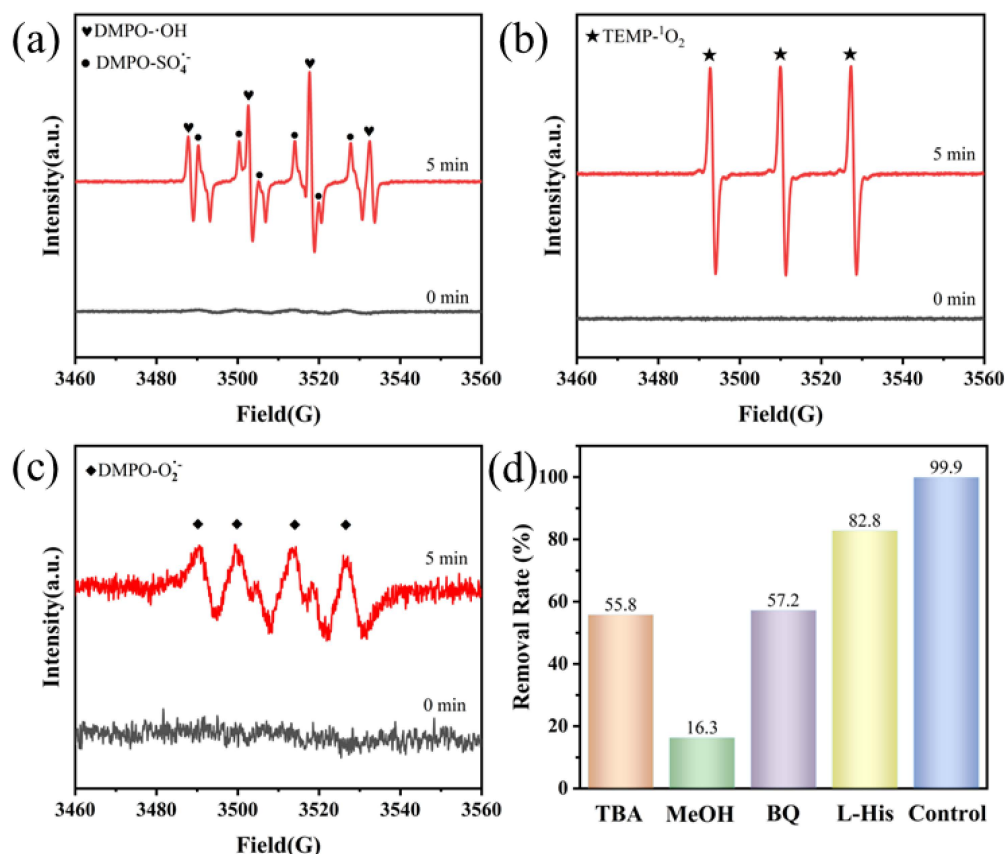
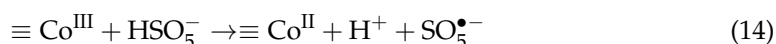
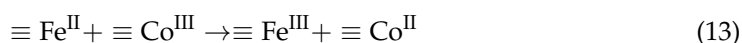
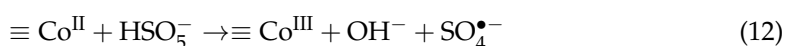
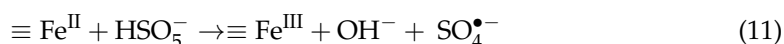
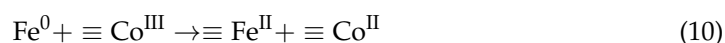
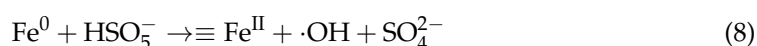


Figure 11. (a) EPR spectra of $\text{SO}_4^{\cdot-}$ and $\cdot\text{OH}$ captured by DMPO; (b) EPR spectra captured by DMPO $\cdot\text{O}_2^{\cdot-}$; (c) EPR spectra of $^1\text{O}_2$ captured by TEMP; (d) quenching experiments.

To further identify the active components in the reaction system, the ROS generated during the catalytic degradation process were determined by EPR spectroscopic detection [55]. In this process, DMPO and TEMP were selected as the trapping agents that are capable of efficiently trapping and labeling radicals such as $\text{SO}_4^{\cdot-}$, $\cdot\text{OH}$, $\cdot\text{O}_2^{\cdot-}$, and $^1\text{O}_2$. As shown in Figure 11a, when DMPO was used as the spin trapping agent, no significant changes in the $\text{SO}_4^{\cdot-}$ radicals were observed at 0 min with only the addition of catalyst and no PMS present. After 5 min of adding PMS, significant characteristic signal peaks for $\text{SO}_4^{\cdot-}$ and $\cdot\text{OH}$ were observed where the intensity ratio of DMPO- $\cdot\text{OH}$ was about 1:2:2:1, which can be attributed to the hyperfine splitting of DMPOX [56]. Similarly, no corresponding characteristic peaks were observed at 0 min, but after 5 min of PMS addition, a broad quadruple peak of DMPO- $\cdot\text{O}_2^{\cdot-}$ was observed, as shown in Figure 11c. TEMP was employed as the spin trapping agent, and according to the results in Figure 11b, a distinct triplet signal peak with an intensity ratio of 1:1:1 was observed at 5 min in the catalyst/PMS/TEMP system, which can be attributed to the characteristic peak of $^1\text{O}_2$. The analysis of the EPR results showed the presence of $\text{SO}_4^{\cdot-}$, $\cdot\text{OH}$, $\cdot\text{O}_2^{\cdot-}$, and $^1\text{O}_2$, which corresponded to the quenching experimental results. In conclusion, CoFe@CSC-700 can rapidly activate PMS and promote the decomposition of PMS molecules and the release of $^1\text{O}_2$.

Combined with analyses such as reaction XPS and EPR, the mechanism of LEV degradation by CoFe@CSC-700/PMS system can be roughly deduced. The redox potentials of $\text{Fe}^0/\equiv\text{Fe}^{\text{II}}$ and $\equiv\text{Fe}^{\text{II}}/\equiv\text{Fe}^{\text{III}}$ are 0.44 V and 0.77 V, respectively, whereas that of $\equiv\text{Co}^{\text{II}}/\equiv\text{Co}^{\text{III}}$ is 1.81 V. Therefore, Fe^0 can provide electrons to $\equiv\text{Co}^{\text{III}}$ and $\equiv\text{Fe}^{\text{III}}$ [57]. From Equation 8, Fe^0 can activate PMS to generate $\cdot\text{OH}$, while Fe^0 can reduce $\equiv\text{Fe}^{\text{III}}/\equiv\text{Co}^{\text{III}}$ to $\equiv\text{Fe}^{\text{II}}$ and $\equiv\text{Co}^{\text{II}}$ as shown in Equations (9) and (10) [56]. Furthermore, since the redox potentials of $\text{HSO}_5^{\cdot-}/\text{SO}_5^{\cdot-}$ and $\text{HSO}_5^{\cdot-}/\text{SO}_4^{\cdot-}$ are 1.1 V and 2.5–3.1 V, respectively, and the redox potential of $\equiv\text{Co}^{\text{II}}/\equiv\text{Co}^{\text{III}}$ (1.81 V) is in between, thermodynamically, the activation of PMS becomes possible [58,59]. PMS acts as an oxidizing agent and a reducing agent at

the same time, participating in the $\equiv\text{Co}^{\text{II}}/\equiv\text{Co}^{\text{III}}$ cycle [60]. Since $\equiv\text{Co}^{\text{II}}/\equiv\text{Co}^{\text{III}}$ has a low redox potential relative to $\equiv\text{Fe}^{\text{II}}/\equiv\text{Fe}^{\text{III}}$, $\equiv\text{Fe}^{\text{II}}$ can also transfer electrons to $\equiv\text{Co}^{\text{III}}$, allowing the reduction of $\equiv\text{Co}^{\text{III}}$ to $\equiv\text{Co}^{\text{II}}$. Also, $\equiv\text{Fe}^{\text{II}}$ can activate PMS to produce $\text{SO}_4^{\cdot-}$, but there is an undesirable reaction between $\equiv\text{Fe}^{\text{III}}$ and PMS, since compared to $\text{HSO}_5^-/\text{SO}_5^{\cdot-}$, the redox potentials $\equiv\text{Fe}^{\text{II}}/\equiv\text{Fe}^{\text{III}}$ are both negative compared to $\text{SO}_5^{\cdot-}$, and the reaction is not thermodynamically feasible. Therefore, the redox reactions and cycles in $\text{Fe}^0/\equiv\text{Fe}^{\text{II}}/\equiv\text{Fe}^{\text{III}}$ and $\equiv\text{Co}^{\text{II}}/\equiv\text{Co}^{\text{III}}$ activate PMS, which continuously generates ROS. In addition, O_2 in water traps electrons to generate $\cdot\text{O}_2^-$, and some of the $\text{SO}_5^{\cdot-}$ can further react with H_2O to generate $^1\text{O}_2$. Thus, in the presence of these highly reactive $\text{SO}_4^{\cdot-}$, $\cdot\text{OH}$, and $\cdot\text{O}_2^-$ radicals and $^1\text{O}_2$, the degradation of LEV by CoFe@CSC-700-catalyst-activated PMS was achieved. Based on the above analysis results, the mechanism of LEV degradation by the CoFe@CSC-700/PMS system is revealed, and the specific reaction mechanism process is shown in the following equations:



3.5. LEV Degradation Products and Pathways

To explore the potential degradation pathways of LEV in the CoFe@CSC-700/PMS system, LC-MS was utilized to identify the intermediates produced during LEV degradation in the system. According to the mass spectrum information obtained by the test and related reports, the spectrum of the intermediate product of LEV partial degradation (Figure 12) and the possible LEV degradation pathway (Figure 13) could be obtained. On this basis, four possible pathways were proposed. The first pathway was the disconnection of the piperazine ring to generate N-methylpiperazine with $m/z = 101$ [61]. The second pathway was the destruction of the N-methyl group on the piperazine ring of LEV and oxidation of the N-methyl group to the carboxyl group by ROS to generate the $m/z = 392$ degradation product, which was subsequently dehydrated to generate N-formyl LEV ($m/z = 376$), and then decarboxylation and the disconnection of piperazine took place to generate $m/z = 202$. Then, demethylation finally produced degradation products with $m/z = 188$ [62]. The third pathway involved the removal of the N-methyl group from the piperazine ring of LEV generating a degradation product with $m/z = 348$, followed by the N oxidation of the piperazine ring to a hydroxylamine generating a degradation product with $m/z = 364$, and subsequently, the removal of hydroxyl generated a degradation product with $m/z = 346$, which was subsequently decarboxylated to generate a degradation product with $m/z = 288$ [63]. The fourth pathway involved the oxidative ring opening of the LEV piperazine ring to generate a bis-N-formyl LEV ($m/z = 392$), followed by the removal of the two formyl groups to generate a degradation product with $m/z = 336$, followed by the removal of the N-methyl group to generate a degradation product with $m/z = 322$, followed by the removal of methylamino group to generate a degradation product with $m/z = 279$, followed by the removal of the amino group and the removal of fluorine to generate a degradation product with $m/z = 262$ [64]. All these intermediates can be

further decomposed into other smaller molecules of organic and inorganic compounds and eventually mineralized into water and carbon dioxide.

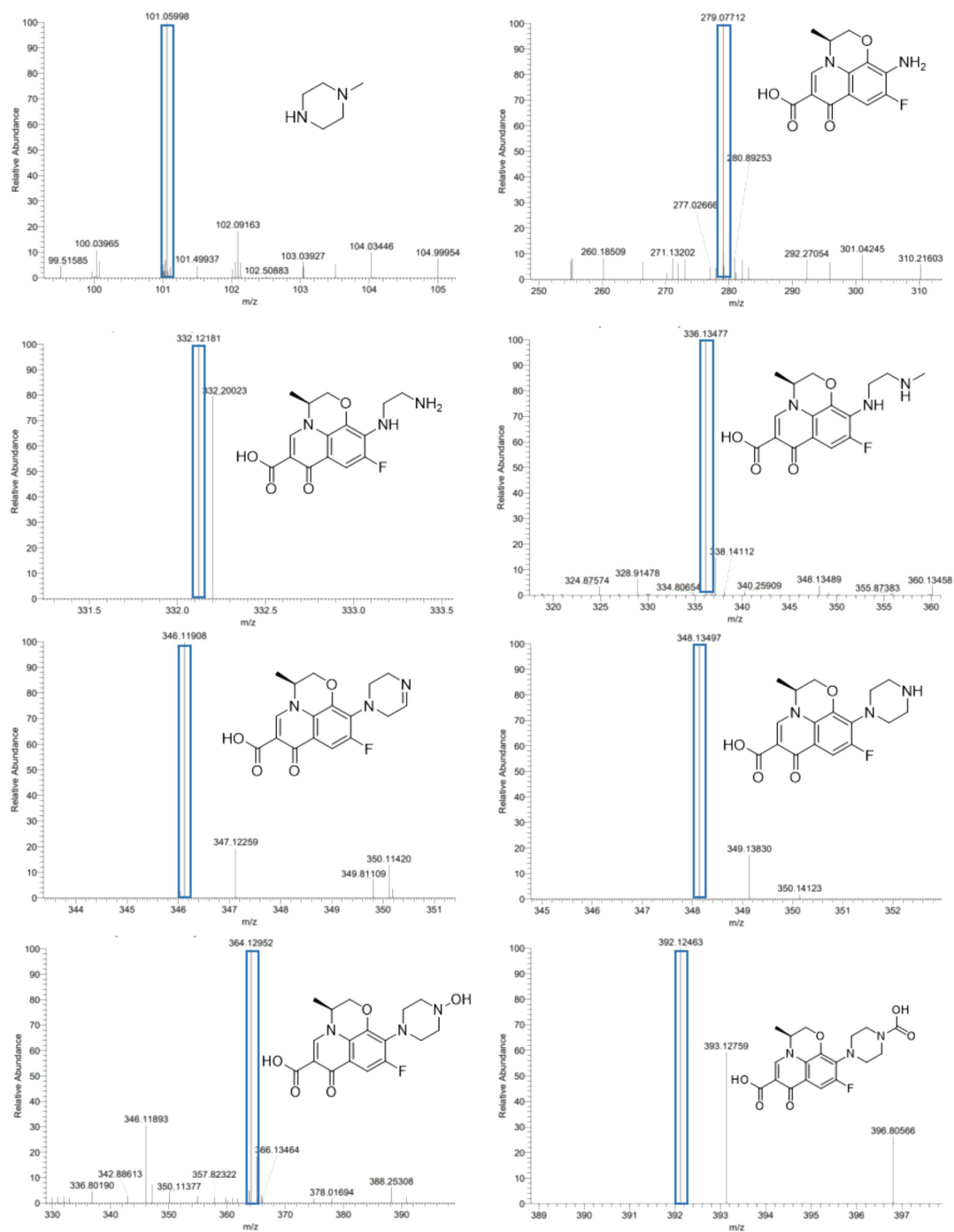


Figure 12. Spectrum of partial intermediate products for activated persulfate degradation of LEV.

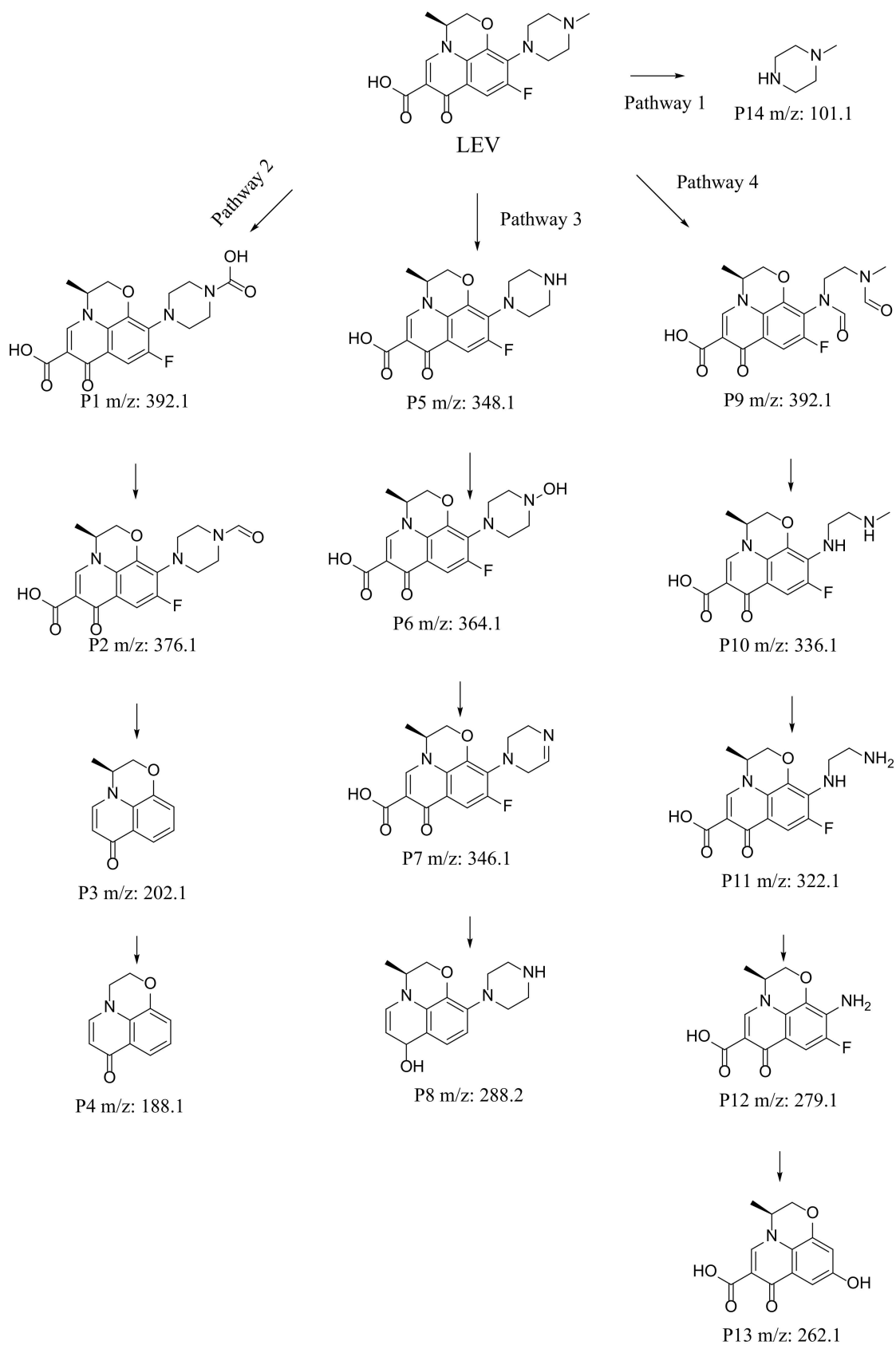


Figure 13. Possible pathways for LEV degradation in CoFe@CSC-700/PMS system.

3.6. Toxicity Analysis

In order to reveal whether LEV and its degradation products in this study pose a threat to human health or not, the developmental toxicity and mutagenicity of the LEV and intermediates were predicted by quantitative structure–activity relationship (QSAR) using Toxicity Estimation Software Tool (T.E.S.T). As shown in Figure 14, LEV was considered developmentally toxic (1.03) and mutagenicity positive (0.65). The toxicity of the intermediates changed as the degradation reaction progressed. As shown in Figure 14a, the developmental toxicity of the intermediates of P7 and P13 was slightly higher than that of LEV, while the developmental toxicity of all the other intermediates was reduced, with P14 being non-toxic (0.49), which implies a reduction in toxicity. In addition, except for P13, P9, and P2, the mutagenicity results showed reduced toxicity for other intermediates, and the P8 and P14 intermediates showed negative mutagenicity (Figure 14b). Therefore, the overall biotoxicity of the intermediates in the PMS-catalyzed system was reduced compared to LEV, indicating that the catalytic degradation of LEV by the CoFe@CSC-700/PMS system is an environmentally friendly process.

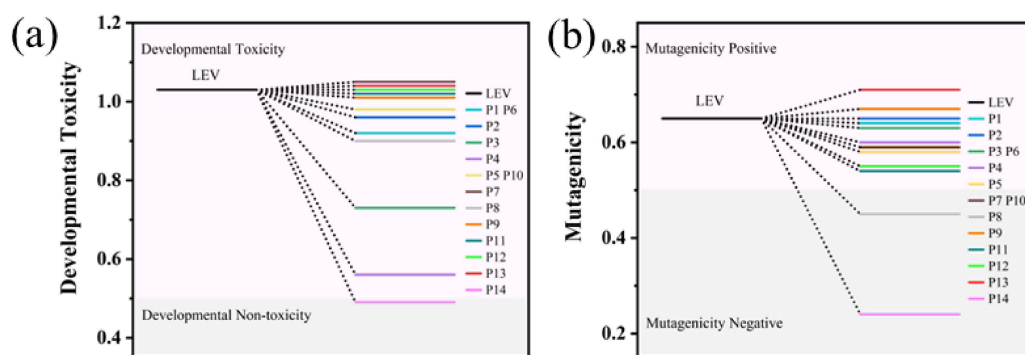


Figure 14. QSAR analysis based on (a) developmental toxicity and (b) mutagenicity.

4. Conclusions

In summary, the CoFe@CSC-700 microspheres prepared in this study were mainly composed of CoFe alloy and graphitized carbon, which were microspheres of about 1 mm with an apparent “core–shell” structure, and the calcined chitosan acted as a protective coating for the CoFe alloy. The CoFe@CSC-700 had a high degree of graphitization ($I_D/I_G = 0.921$) resulting in excellent properties. Under the conditions of pH = 6.8, PMS = 0.1 g/L, and CoFe@CSC-700 = 0.1 g/L, the degradation of LEV was nearly complete within 30 min, and the metal leaching was in accordance with national standards. CoFe@CSC-700 showed excellent activity after five cycles, and more than 90% degradation efficiency was maintained. During the catalytic reaction, the relevant redox reactions of $\text{Fe}^0/\equiv\text{Fe}^{\text{II}}/\equiv\text{Fe}^{\text{III}}$ and $\equiv\text{Co}^{\text{II}}/\equiv\text{Co}^{\text{I}}$ activated PMS. The quenching experiment and EPR test results indicated the involvement of $\text{SO}_4^{\cdot-}$, $\cdot\text{OH}$, $\cdot\text{O}_2^-$, and $^1\text{O}_2$ in the degradation process of LEV, with $\text{SO}_4^{\cdot-}$, $\cdot\text{OH}$, and $\cdot\text{O}_2^-$ playing a leading role and $^1\text{O}_2$ also contributing to the degradation of LEV. Four possible degradation pathways were postulated by LC-MS analysis. CoFe@CSC-700 exhibited outstanding catalytic activity, as well as remarkable reusability and recyclability. This study provides a potential method for preparing bimetallic catalysts that are easy to separate and recover for application in AOPs.

Supplementary Materials: The following supporting information can be downloaded at <https://www.mdpi.com/article/10.3390/w16131818/s1>: Figure S1: Zeta potential of CoFe@CSC-700; Table S1: Comparisons of CoFe@CSC-700 with other catalysts for the degradation of LEV.

Author Contributions: T.H.: conceptualization, experiment setup, sampling, investigation, writing—original draft and editing. Y.C., X.G. and Y.P.: investigation, formal analysis, data curation. J.C.: conceptualization, methodology, writing—review and editing, funding acquisition. All authors have read and agreed to the published version of the manuscript.

Funding: This work was financed by the National Natural Science Foundation of China (No. 21976060), the Dongguan Social Science and Technology Development Project (20221800905482).

Data Availability Statement: The original contributions presented in the study are included in the article/Supplementary Materials, further inquiries can be directed to the corresponding author.

Conflicts of Interest: The authors declare no conflicts of interest.

References

- Niu, J.; Chen, Y.; Li, X.; Lin, J.; Cheng, J.; Hu, Y. A “sandwich layer” of N-doped carbon nanotubes coated on the surface of oxidized iron-foam is used to drive peroxymonosulfate activation. *Sep. Purif. Technol.* **2023**, *311*, 123273. [\[CrossRef\]](#)
- Aldred, K.J.; Kerns, R.J.; Osherooff, N. Mechanism of quinolone action and resistance. *Biochemistry* **2014**, *53*, 1565–1574. [\[CrossRef\]](#) [\[PubMed\]](#)
- Yang, Y.; Li, H.; Hou, Y.L.; Wang, C.; Zhang, K.Y.; Man, Z.H.; Shang, J.W.; Cheng, X.W. Green synthesis of Co-Ce ZIF derivatives for enhanced O₃/PMS degradation of levofloxacin. *J. Environ. Chem. Eng.* **2024**, *12*, 112158. [\[CrossRef\]](#)
- Guerra-Rodríguez, S.; Rodríguez, E.; Singh, D.N.; Rodríguez-Chueca, J. Assessment of Sulfate Radical-Based Advanced Oxidation Processes for Water and Wastewater Treatment: A Review. *Water* **2018**, *10*, 1828. [\[CrossRef\]](#)
- Wang, J.; Wang, Q.; Gao, P.; Sun, D.; Jin, L.; Ma, L.; Yang, L.; Zhao, J. Enhanced PMS Activation by Highly Dispersed Mn-Ce Bimetallic Oxide on Carbon Nanotubes for Degradation of Phenol. *Water* **2023**, *15*, 2243. [\[CrossRef\]](#)
- Wang, C.; Zhou, G.; Xu, Y.; Yu, P.; Sun, Y. Nitrogen Doped Cobalt Anchored on the Used Resin-Based Catalyst to Activate Peroxymonosulfate for the Removal of Ibuprofen. *Water* **2022**, *14*, 3754. [\[CrossRef\]](#)
- Mo, Y.; Xu, W.; Zhang, X.; Zhou, S. Enhanced Degradation of Rhodamine B through Peroxymonosulfate Activated by a Metal Oxide/Carbon Nitride Composite. *Water* **2022**, *14*, 2054. [\[CrossRef\]](#)
- Huang, K.C.; Zhao, Z.; Hoag, G.; Dahmani, A.; Block, P. Degradation of volatile organic compounds with thermally activated persulfate oxidation. *Chemosphere* **2005**, *61*, 551–560. [\[CrossRef\]](#) [\[PubMed\]](#)
- Qi, C.D.; Liu, X.T.; Ma, J.; Lin, C.Y.; Li, X.W.; Zhang, H.J. Activation of peroxymonosulfate by base: Implications for the degradation of organic pollutants. *Chemosphere* **2016**, *151*, 280–288. [\[CrossRef\]](#)
- Kohantorabi, M.; Moussavi, G.; Giannakis, S. A review of the innovations in metal- and carbon-based catalysts explored for heterogeneous peroxymonosulfate (PMS) activation, with focus on radical vs. non-radical degradation pathways of organic contaminants. *Chem. Eng. J.* **2021**, *411*, 127957. [\[CrossRef\]](#)
- He, X.; Mezyk, S.P.; Michael, I.; Fatta-Kassinos, D.; Dionysiou, D.D. Degradation kinetics and mechanism of beta-lactam antibiotics by the activation of H₂O₂ and Na₂S₂O₈ under UV-254 nm irradiation. *J. Hazard. Mater.* **2014**, *279*, 375–383. [\[CrossRef\]](#) [\[PubMed\]](#)
- Fan, Y.; Ji, Y.; Zheng, G.; Lu, J.; Kong, D.; Yin, X.; Zhou, Q.S. Degradation of atrazine in heterogeneous Co₃O₄ activated peroxymonosulfate oxidation process: Kinetics, mechanisms, and reaction pathways. *Chem. Eng. J.* **2017**, *330*, 831–839. [\[CrossRef\]](#)
- Hao, F.; Guo, W.; Wang, A.; Leng, Y.; Li, H. Intensification of sonochemical degradation of ammonium perfluorooctanoate by persulfate oxidant. *Ultrason. Sonochem.* **2014**, *21*, 554–558. [\[CrossRef\]](#) [\[PubMed\]](#)
- Chen, C.; Liu, L.; Li, Y.X.; Li, W.; Zhou, L.X.; Lan, Y.Q.; Li, Y. Insight into heterogeneous catalytic degradation of sulfamethazine by peroxymonosulfate activated with CuCo₂O₄ derived from bimetallic oxalate. *Chem. Eng. J.* **2020**, *384*, 123257. [\[CrossRef\]](#)
- Huang, J.Z.; Zhang, H.C. Mn-based catalysts for sulfate radical-based advanced oxidation processes: A Review. *Environ. Int.* **2019**, *133*, 105141. [\[CrossRef\]](#) [\[PubMed\]](#)
- Yang, Q.J.; Choi, H.; Al-Abed, S.R.; Dionysiou, D.D. Iron–cobalt mixed oxide nanocatalysts: Heterogeneous peroxymonosulfate activation, cobalt leaching, and ferromagnetic properties for environmental applications. *Appl. Catal. B Environ.* **2009**, *88*, 462–469. [\[CrossRef\]](#)
- Zhou, X.Q.; Luo, C.G.; Luo, M.G.; Wang, Q.L.; Wang, J.; Liao, Z.W.; Chen, Z.L.; Chen, Z.Q. Understanding the synergetic effect from foreign metals in bimetallic oxides for PMS activation: A common strategy to increase the stoichiometric efficiency of oxidants. *Chem. Eng. J.* **2020**, *381*, 122587. [\[CrossRef\]](#)
- Zhou, R.; Zhao, J.; Shen, N.F.; Ma, T.G.; Su, Y. Efficient degradation of 2,4-dichlorophenol in aqueous solution by peroxymonosulfate activated with magnetic spinel FeCo₂O₄ nanoparticles. *Chemosphere* **2018**, *197*, 670–679. [\[CrossRef\]](#) [\[PubMed\]](#)
- Pujol, A.A.; Leo'n, I.; Ca'rdenas, J.; Sepúlveda-Guzmán, S.; Manríquez, J.; Sirés, I.; Bustos, E. Degradation of phenols by heterogeneous electro-Fenton with a Fe₃O₄-chitosan composite and a boron-doped diamond anode. *Electrochim. Acta* **2020**, *337*, 135784. [\[CrossRef\]](#)
- Baran, T. Pd NPs@Fe₃O₄/chitosan/pumice hybrid beads: A highly active, magnetically retrievable, and reusable nanocatalyst for cyanation of aryl halides. *Carbohydr. Polym.* **2020**, *237*, 116105. [\[CrossRef\]](#)
- Chen, X.; Xu, X.J.; Zheng, X.C.; Guan, X.X.; Liu, P.U. Chitosan supported palladium nanoparticles: The novel catalysts for hydrogen generation from hydrolysis of ammonia borane. *Mater. Res. Bull.* **2018**, *103*, 89–95. [\[CrossRef\]](#)
- Shang, Z.X.; Chen, Z.L.; Zhang, Z.B.; Yu, J.; Tan, S.Z. CoFe nanoalloy particles encapsulated in nitrogen-doped carbon layers as bifunctional oxygen catalyst derived from a Prussian blue analogue. *J. Alloy. Compd.* **2018**, *740*, 743–753. [\[CrossRef\]](#)
- Ge, B.C.; Li, K.X.; Fu, Z.; Pu, L.T.; Zhang, X. The addition of ortho-hexagon nano spinel Co₃O₄ to improve the performance of activated carbon air cathode microbial fuel cell. *Bioresour. Technol.* **2015**, *95*, 180–187. [\[CrossRef\]](#) [\[PubMed\]](#)

24. Wang, Y.; Wang, H.; Ye, J.; Shi, L.; Feng, X. Magnetic CoFe alloy@C nanocomposites derived from ZnCo-MOF for electromagnetic wave absorption. *Chem. Eng. J.* **2020**, *383*, 123096. [\[CrossRef\]](#)
25. Zakaria, M.B.; Chikyow, T. Recent advances in Prussian blue and Prussian blue analogues: Synthesis and thermal treatments. *Coord. Chem. Rev.* **2017**, *352*, 328–345. [\[CrossRef\]](#)
26. Li, M.Q.; Luo, R.; Wang, C.H.; Zhang, M.; Zhang, W.X.; Klu, P.K.; Yan, Y.B.; Qi, J.W.; Sun, X.Y.; Wang, L.J.; et al. Iron-tannic modified cotton derived Fe⁰/graphitized carbon with enhanced catalytic activity for bisphenol A degradation. *Chem. Eng. J.* **2019**, *372*, 774–784. [\[CrossRef\]](#)
27. Shang, Y.N.; Chen, C.; Zhang, P.; Yue, Q.Y.; Li, Y.W.; Gao, B.Y.; Xu, X. Removal of sulfamethoxazole from water via activation of persulfate by Fe₃C@NCNTs including mechanism of radical and nonradical process. *Chem. Eng. J.* **2019**, *375*, 122004. [\[CrossRef\]](#)
28. Dresselhaus, M.S.; Jorio, A.; Hofmann, M.; Dresselhaus, G.; Saito, R. Perspectives on carbon nanotubes and graphene Raman spectroscopy. *Nano. Lett.* **2010**, *10*, 751–758. [\[CrossRef\]](#) [\[PubMed\]](#)
29. Xu, D.Y.; Liu, B.B.; Liu, G.Y.; Su, K.D.; Li, J.H. N-doped bamboo-like CNTs combined with CoFe-CoFe₂O₄ as a highly efficient electrocatalyst towards oxygen evolution. *Int. J. Hydrogen Energy* **2020**, *45*, 6629–6635. [\[CrossRef\]](#)
30. Zhang, L.J.; Su, Z.X.; Jiang, F.L.; Yang, L.L.; Qian, J.J.; Zhou, Y.Y.; Li, W.M.; Hong, M.C. Highly graphitized nitrogen-doped porous carbon nanopolyhedra derived from ZIF-8 nanocrystals as efficient electrocatalysts for oxygen reduction reactions. *Nanoscale* **2014**, *6*, 6590–6602. [\[CrossRef\]](#)
31. Duan, X.G.; Ao, Z.M.; Li, D.G.; Sun, H.Q.; Suvorova, A.; Saunders, M.; Wang, G.X.; Wan, S.B. Surface-tailored nanodiamonds as excellent metal-free catalysts for organic oxidation. *Carbon* **2016**, *103*, 404–411. [\[CrossRef\]](#)
32. Huo, L.M.; Wang, T.; Xuan, K.; Li, L.; Pu, Y.F.; Li, C.X.; Qiao, C.Z.; Yang, H.; Bai, Y. Synthesis of dimethyl carbonate from CO₂ and methanol over Zr-based catalysts with different chemical environments. *Catalysts* **2021**, *11*, 710. [\[CrossRef\]](#)
33. Zhou, X.C.; Chen, S.Q.; Zhou, M.J.; Li, M.; Lan, S.; Feng, T. Highly efficient cobalt-based amorphous catalyst for peroxymonosulfate activation toward wastewater remediation. *Rare Met.* **2023**, *42*, 1160–1174. [\[CrossRef\]](#)
34. Zhao, L.; Li, W.; Lin, L.; Guo, W.; Zhao, W.; Tang, X.; Gong, D.; Li, Q.; Xu, P. Field investigation on river hydrochemical characteristics and larval and juvenile fish in the source region of the Yangtze River. *Water* **2019**, *11*, 1342. [\[CrossRef\]](#)
35. Mashentseva, A.A.; Aimanova, N.A.; Parmanbek, N.; Temirgazyev, B.S.; Barsbay, M.; Zdorovets, M.V. Serratula coronata L. mediated synthesis of ZnO nanoparticles and their application for the removal of alizarin Yellow R by photocatalytic degradation and adsorption. *Nanomaterials* **2022**, *12*, 3293. [\[CrossRef\]](#) [\[PubMed\]](#)
36. Deng, J.; Feng, S.F.; Ma, X.; Tan, C.; Wang, H.; Zhou, S.; Zhang, T.; Li, J. Heterogeneous degradation of Orange II with peroxymonosulfate activated by ordered mesoporous MnFe₂O₄. *Sep. Purif. Technol.* **2016**, *167*, 181–189. [\[CrossRef\]](#)
37. Zeng, Q.Y.; Tan, J.; Gao, B.B.; Cai, T.; Zhang, Q.Y.; Liu, Y.L.; Chang, S.; Zhao, S.F.; Wu, S.Q. Embedding Co in perovskite MoO₃ for superior catalytic oxidation of refractory organic pollutants with peroxymonosulfate. *Chemosphere* **2023**, *314*, 137726. [\[CrossRef\]](#)
38. Zhao, W.; Duan, Z.Y.; Zheng, Z.; Li, B. Cobalt bismuth oxide with cobalt(II/III) as a new stable peroxymonosulfate activator for effective degradation, mineralization, and detoxification of diclofenac in water. *J. Clean. Prod.* **2023**, *365*, 132781. [\[CrossRef\]](#)
39. Zhu, S.J.; Wang, Z.W.; Ye, C.; Deng, J.; Ma, X.Y.; Xu, Y.P.; Wang, L.; Tang, Z.; Luo, H.; Li, X.Y. Magnetic Co/Fe nanocomposites derived from ferric sludge as an efficient peroxymonosulfate catalyst for ciprofloxacin degradation. *Chem. Eng. J.* **2022**, *432*, 134180. [\[CrossRef\]](#)
40. Yuan, R.X.; Jiang, M.L.; Gao, S.M.; Wang, Z.H.; Wang, H.Y.; Boczkaj, G.; Liu, Z.J.; Ma, J.; Li, Z.J. 3D mesoporous α-Co(OH)₂ nanosheets electrodeposited on nickel foam: A new generation of macroscopic cobalt-based hybrid for peroxymonosulfate activation. *Chem. Eng. J.* **2020**, *80*, 122447. [\[CrossRef\]](#)
41. Yang, Y.Q.; Ji, W.Q.; Li, X.Y.; Lin, H.D.; Chen, H.J.; Bi, F.K.; Zheng, Z.H.; Xu, J.C.; Zhang, X.D. Insights into the mechanism of enhanced peroxymonosulfate degraded tetracycline using metal organic framework derived carbonyl modified carbon-coated Fe⁰. *J. Hazard. Mater.* **2022**, *424*, 127640. [\[CrossRef\]](#) [\[PubMed\]](#)
42. Cheng, M.; Ma, R.; Chai, G.; Chen, Y.; Bai, L.; Wang, D.; Qian, J.; Chen, G.H. Nitrogen-doped carbonized polyaniline(N-CPANI) for peroxydisulfate(PDS) activation towards efficient degradation of doxycycline(DOX) via the non-radical pathway dominated by electron transfer. *Chem. Eng. J.* **2023**, *453*, 139810. [\[CrossRef\]](#)
43. Wang, A.Q.; Zheng, Z.K.; Wang, H.; Chen, Y.W.; Luo, C.H.; Liang, D.J.; Hu, B.; Qiu, R.L.; Yan, K. 3D hierarchical H₂-reduced Mn-doped CeO₂ microflowers assembled from nanotubes as a high-performance Fenton-like photocatalyst for tetracycline antibiotics degradation. *Appl. Catal. B-Environ.* **2020**, *277*, 119171. [\[CrossRef\]](#)
44. Ye, F.; Su, Y.M.; Li, R.P.; Sun, W.; Pu, M.J.; Yang, C.; Yang, W.C.; Huang, H.M.; Zhang, Q.C.; Wong, J.W.C. Activation of persulfate on fluorinated carbon: Role of semi-ionic C-F in inducing mechanism transition from radical to electron-transfer nonradical pathway. *Appl. Catal. B-Environ.* **2023**, *337*, 122992. [\[CrossRef\]](#)
45. Zhang, Z.; Dai, Y.Z. Co₃O₄/C-PC composite derived from pomelo peel-loaded ZIF-67 for activating peroxymonosulfate(PMS) to degrade ciprofloxacin. *J. Water Process. Eng.* **2022**, *49*, 103043. [\[CrossRef\]](#)
46. Zhong, Y.W.; Shih, K.M.; Diao, Z.H.; Gang, S.; Su, M.H.; Hou, L.A.; Chen, D.Y.; Kong, L.J. Peroxymonosulfate activation through LED-induced ZnFe₂O₄ for levofloxacin degradation. *Chem. Eng. J.* **2021**, *417*, 129225–129235. [\[CrossRef\]](#)
47. Pi, Y.Q.; Gao, H.Q.; Cao, Y.D.; Cao, R.L.; Wang, Y.B.; Sun, J.H. Cobalt ferrite supported on carbon nitride matrix prepared using waste battery materials as a peroxymonosulfate activator for the degradation of levofloxacin hydrochloride. *Chem. Eng. J.* **2020**, *379*, 122377–122385. [\[CrossRef\]](#)

48. Liu, L.L.; Zhan, R.; Zhang, M.; Li, J.N.; Wang, Z.P.; Mi, H.S.; Zhang, Y.X. Insights into the performance, mechanism, and ecotoxicity of levofloxacin degradation in CoFe_2O_4 catalytic peroxymonosulfate process. *J. Environ. Chem. Eng.* **2022**, *10*, 107435–107445. [\[CrossRef\]](#)
49. Zhao, J.; Xiao, P.F.; Han, S.; Zulhumar, M.; Wu, D.D. Preparation of magnetic copper ferrite nanoparticle as peroxymonosulfate activating catalyst for effective degradation of levofloxacin. *Water Sci. Technol.* **2022**, *85*, 645–663. [\[CrossRef\]](#)
50. Zhao, Q.Z.; Wu, Y.Z.; Zhang, X.X.; Zhou, L.; Lu, S.; Zhang, J.L.; Liu, Y.D.; Lei, J.Y. Enhanced PMS activation by Mn_2O_3 -loaded h-BN for levofloxacin removal: Unveiling the dominant influence of non-free radical pathway and N-Mn-mediated promotion of stable, long-lived Mn(IV) species. *Appl. Surf. Sci.* **2024**, *657*, 159716. [\[CrossRef\]](#)
51. Li, M.K.; Huang, F.L.; Hu, L.; Sun, W.; Li, E.P.; Xiong, D.L.; Zhong, H.; He, Z.G. Efficient activation of peroxymonosulfate by a novel catalyst prepared directly from electrolytic manganese slag for degradation of recalcitrant organic pollutants. *Chem. Eng. J.* **2020**, *401*, 126085. [\[CrossRef\]](#)
52. He, Y.X.; Qian, J.; Wang, P.F.; Wu, J.; Lu, B.H.; Tang, S.J.; Gao, P. Acceleration of levofloxacin degradation by combination of multiple free radicals via MoS_2 anchored in manganese ferrite doped perovskite activated PMS under visible light. *Chem. Eng. J.* **2022**, *431*, 133933. [\[CrossRef\]](#)
53. Yuan, S.H.; Liao, P.; Alshawabkeh, A.N. Electrolytic manipulation of persulfate reactivity by iron electrodes for trichloroethylene degradation in groundwater. *Environ. Sci. Technol.* **2014**, *48*, 656–663. [\[CrossRef\]](#)
54. Chen, L.W.; Zuo, X.; Zhou, L.; Huang, Y.; Yang, S.J.; Cai, T.M.; Ding, D.H. Efficient heterogeneous activation of peroxymonosulfate by facilely prepared Co/Fe bimetallic oxides: Kinetics and mechanism. *Chem. Eng. J.* **2018**, *345*, 364–374. [\[CrossRef\]](#)
55. Zhu, J.L.; Wang, J.; Shan, C.; Zhang, J.; Lv, L.; Pan, B.C. Durable activation of peroxymonosulfate mediated by Co-doped mesoporous FePO_4 via charge redistribution for atrazine degradation. *Chem. Eng. J.* **2019**, *375*, 122009. [\[CrossRef\]](#)
56. Liu, Y.; Guo, H.G.; Zhang, Y.L.; Tang, W.H.; Cheng, X.; Li, W. Heterogeneous activation of peroxymonosulfate by sillenite $\text{Bi}_{25}\text{FeO}_{40}$: Singlet oxygen generation and degradation for aquatic levofloxacin. *Chem. Eng. J.* **2018**, *343*, 128–137. [\[CrossRef\]](#)
57. Sheng, J.L.; Guo, S.K.; Yuan, C.; Nie, X.R.; Cui, P.L.; Jiang, H.M. Degradation of bisulfuron-methyl by magnetic CoFe alloy@N-doped graphitized carbon derived from CoFe_2O_4 activated by peroxymonosulfate. *Chem. Eng. J.* **2023**, *466*, 143158. [\[CrossRef\]](#)
58. Su, S.N.; Guo, W.L.; Leng, Y.Q.; Yi, C.L.; Ma, Z.M. Heterogeneous activation of Oxone by $\text{Co}_x\text{Fe}_{3-x}\text{O}_4$ nanocatalysts for degradation of rhodamine B. *J. Hazard. Mater.* **2013**, *244–245*, 736–742. [\[CrossRef\]](#)
59. Ma, W.J.; Wang, N.; Du, Y.C.; Tong, T.Z.; Zhang, L.J.; Andrew Lin, K.Y.; Han, X.J. One-step synthesis of novel Fe_3C @nitrogen-doped carbon nanotubes/graphene nanosheets for catalytic degradation of Bisphenol A in the presence of peroxymonosulfate. *Chem. Eng. J.* **2019**, *356*, 1022–1031. [\[CrossRef\]](#)
60. Li, X.N.; Rykov, A.I.; Zhang, B.; Zhang, Y.J.; Wang, J.H. Graphene encapsulated Fe_xCo_y nanocages derived from metal-organic frameworks as efficient activators for peroxymonosulfate. *Catal. Sci. Technol.* **2016**, *6*, 7486–7494. [\[CrossRef\]](#)
61. Yan, J.W.; Lin, G.; Chai, S.Y.; Guo, C.; Zhang, W.; Wan, H.Y. ZIF-67 loaded lotus leaf-derived biochar for efficient peroxymonosulfate activation for sustained levofloxacin degradation. *Chem. Eng. J.* **2023**, *458*, 141456. [\[CrossRef\]](#)
62. Zhang, G.S.; Wang, Y.; Chen, M.; Xu, J.X.; Wang, L. ZIF-67-derived carbon@ Co_3S_4 / CoSO_4 /MnO polyhedron to activate peroxymonosulfate for degrading levofloxacin: Synergistic effect and mechanism. *Chem. Eng. J.* **2023**, *451*, 138976. [\[CrossRef\]](#)
63. Xue, X.J.; Liao, W.D.; Liu, D.L.; Zhang, X.D.; Huang, Y.M. $\text{MgO}/\text{Co}_3\text{O}_4$ composite activated peroxymonosulfate for levofloxacin degradation: Role of surface hydroxyl and oxygen vacancies. *Sep. Purif. Technol.* **2023**, *306*, 122560. [\[CrossRef\]](#)
64. Deng, Q.C.; Zhang, X.D.; Chang, L.; Chai, H.X.; Huang, Y.M. The MOF/LDH derived heterostructured $\text{Co}_3\text{O}_4/\text{MnCo}_2\text{O}_4$ composite for enhanced degradation of levofloxacin by peroxymonosulfate activation. *Sep. Purif. Technol.* **2022**, *294*, 121182. [\[CrossRef\]](#)

Disclaimer/Publisher's Note: The statements, opinions and data contained in all publications are solely those of the individual author(s) and contributor(s) and not of MDPI and/or the editor(s). MDPI and/or the editor(s) disclaim responsibility for any injury to people or property resulting from any ideas, methods, instructions or products referred to in the content.